



Thermal conductivity of surficial lunar regolith estimated from Lunar Reconnaissance Orbiter Diviner Radiometer data

Shuoran Yu^{a,*}, Wenzhe Fa^b

^a Space Science Institute, Macau University of Science and Technology, Macau SAR, China

^b Institute of Remote Sensing and Geographical Information System, Peking University, Beijing 100871, China

ARTICLE INFO

Article history:

Received 11 April 2015

Received in revised form

29 January 2016

Accepted 1 February 2016

Available online 10 February 2016

Keywords:

Moon

Regoliths

Thermal conductivity

Infrared observations

ABSTRACT

The thermal conductivity of lunar regolith is a critical parameter in the determination of surface heat flow and understanding the nature of surface material. As a refinement on this thermophysical parameter, this study aims to present an estimation on the solid thermal conductivity of surficial lunar regolith based on the data of Lunar Reconnaissance Orbiter (LRO) Diviner radiometer. Theoretically, the thermal conductivity of lunar regolith is composed of solid thermal conductivity (i.e. the conductive contribution induced by the interactions among solid grains) and radiative thermal conductivity (i.e. the conductive contribution induced by the inter-granular radiation). The solid thermal conductivity depends on the thermal conductivity of solid grains as well as the effective contact areas among grains, which reflects the nature of lunar surface materials. It is well known that the surface temperature variation in the nighttime is dominated by the thermophysical parameter of surficial lunar regolith. A temperature model based upon heat conductive equation is adopted to correlate the thermophysical parameters of lunar regolith with the surface temperature. Diviner Level-3 bolometric temperature dataset is adopted as the proxy of lunar surface temperature. The estimation is carried out by searching for the optimal surficial solid component that makes the root-mean-square error (RMSE) between Diviner data and simulated temperatures minimum.

The estimation result shows that the solid thermal conductivity of surficial lunar regolith has a wide variation range ($0.0001\text{--}0.0300\text{ W m}^{-1}\text{ K}^{-1}$) between 60°N and 60°S . The solid thermal conductivity on the lunar surface has a prominent latitude dependence, which is doubted as the consequence of the specific surface energy variation versus latitude. In addition, the surface solid thermal conductivity in the older regions is ubiquitously higher than younger regions. This phenomenon would be relative with the variation of grain radius across the entire lunar surface.

In addition, the enrichment of rock abundance at young impact craters makes the estimated solid thermal conductivity abnormally high. We also find a strong correlation between the absolute ages and the estimated surficial solid thermal conductivity of these craters. Based upon the fitted relation between them, the exact absolute ages of Crookes and Ohm are determined as 268 and 252 Myr respectively.

© 2016 Elsevier Ltd. All rights reserved.

1. Introduction

The thermal conductivity of lunar regolith is a critical parameter in the determination of surface heat flow. Till now, the knowledge on this parameter derives mainly from Earth-based observations, returned samples and Apollo heat flow experiments in the early time. Meanwhile, it is still unknown whether these data are representative for the realistic conditions on the lunar surface. Jaeger (1953) reviewed the data of early Earth-based observations at microwave and infrared bands and found that

* Corresponding author.

E-mail address: shuoran.yu@icloud.com (S. Yu).

the thermal behavior of surface material is very similar to that of fine dust. Because Earth-based observations can only cover the nearside of the Moon with a coarse spatial resolution, these data only represent the average level in the nearside of the Moon. In Apollo era, several laboratory experiments were carried out in order to measure the thermal conductivity of returned lunar regolith samples (Cremers and Birkebak, 1971; Cremers and Hsia, 1974). However, these data only represent the conditions at those landing sites and it is still uncertain whether these laboratory experiment data are representative for the realistic conditions on the lunar surface or not. In-situ heat flow experiments at Apollo 15 and 17 landing sites estimated the thermal conductivity of sub-surface lunar regolith by inserting probes into the drilled holes (Langseth et al., 1976). However, it still needs to caution that the

temperature probe can compact the surrounding lunar regolith and increase the effective thermal conductivity of lunar regolith considerably (Grott et al., 2010).

Theoretically, the thermal conductivity of lunar regolith is composed of solid thermal conductivity (i.e. the conduction component induced by the interactions among solid grains) and radiative thermal conductivity (i.e. the conduction component achieved through inter-granular thermal radiation) (Presley and Christensen, 1997). Assuming that the solid grains are randomly and closely packed, Gundlach and Blum (2013) develop a theoretical model in which solid thermal conductivity is expressed as the product between the thermal conductivity of solid grains and the effective contact area among them, while radiation thermal conductivity is expressed as a function of temperature. Even though this model can give an exact estimation on the thermal conductivity of lunar regolith, some parameters (e.g. specific surface energy) still lack in accurate calibration.

As a refinement on the previous results, this study aims to estimate the solid thermal conductivity of surficial lunar regolith from the observations of Lunar Reconnaissance Orbiter (LRO) Diviner radiometer. Diviner radiometer observed the thermal emission from lunar surface at thermal-infrared (TIR) band, which is very sensitive to the temperature of lunar surface. Because the nighttime surface temperature is dominated by the thermophysical properties of lunar regolith as well as the rock debris on the lunar surface, the estimation of thermal conductivity can be achieved on the basis of the quantitative relation between surface temperature and the thermophysical properties of lunar regolith.

As the implications of the theoretical thermal conductivity model in Gundlach and Blum (2013), the solid thermal conductivity correlates with the intrinsic properties of solid grains and the effective contact area among them. In this study, we choose the solid thermal conductivity of surficial lunar regolith as the estimation target because this parameter contains more abundant information about the intrinsic properties of lunar regolith. In addition, the remote sensing observations do not perturb the packing style of lunar regolith and the effective contact area among the solid grains, so the estimation from Diviner observations can represent the realistic condition on the lunar surface.

For this purpose, the remaining content is organized as following. As the fundamental of this study, we will review the current data of thermophysical properties of lunar regolith as well as the method in modelling the surface temperature of the Moon in Section 2. In Section 3, the estimation strategy and corresponding feasibility tests will be discussed. In Section 4, we will discuss the estimation results and the characteristics of thermal conductivity distribution on the lunar surface.

2. Temperature of lunar regolith

2.1. Thermophysical properties of lunar regolith

Lunar regolith is a layer of grained fine that loosely packs in near-surface and tends to be compacted tens of centimeter below (Carrier et al., 1991). Therefore, the thermophysical properties of lunar regolith are expected to be the functions of depth. The bulk density of porous materials depends on the density of solid grains G and porosity n and can be expressed as

$$\rho = G(1 - n) \quad (1)$$

Carrier et al. (1991) derived a typical bulk density profile from the experiments on Apollo returned samples. In this model, the bulk density starts from 1300 kg m^{-3} on the surface, increases rapidly within tens of centimeters atop and tends to 1920 kg m^{-3} at subsurface. The density of solid regolith grains (noted by G in

kg m^{-3}) relies on the FeO and TiO_2 abundances (unit: wt%) (Huang and Wicczorek, 2012)

$$G(\text{FeO}, \text{TiO}_2) = 27.3 \times \text{FeO} + 11.0 \times \text{TiO}_2 + 2773 \quad (2)$$

The Lunar Prospector (LP) gamma-ray spectrum data indicate that both FeO and TiO_2 abundances possess extensive variations across the entire lunar surface (Prettyman et al., 2006), which leads to the variation of G within $2900\text{--}3800 \text{ kg m}^{-3}$. Therefore, this parameter cannot be fixed to a constant in the temperature simulation. In addition, it also needs to caution that the gamma-ray spectrum data only represent the composition of near-surface lunar regolith. However, because lunar regolith has been sufficiently gardened during the long-term bombardment history, it is possibly safe to assume that the composition keeps constant with respect to depth. The porosity profile within lunar regolith was poorly constrained in the past. We adopt the following expression to predict this parameter empirically

$$n(z) = n_d - (n_d - n_s) \exp(-z/H) \quad (3)$$

where n_s and n_d are the porosities on the surface and at subsurface respectively, H (unit: m) is a factor that controls the growth rate of porosity in near-surface layer. In this case, the bulk density of lunar regolith can be expressed as

$$\rho(\text{FeO}, \text{TiO}_2, z) = G(\text{FeO}, \text{TiO}_2) \cdot [1 - n(z)] \quad (4)$$

Here we clarify that Eq. (3) is an approximation of the Fermi function in Güttler et al. (2009) and Schräpler et al. (2015)

$$n(p) = n_2 - \frac{n_2 - n_1}{\exp\left(\frac{\log p - \log p_m}{\Delta}\right) + 1} \quad (5)$$

where n_1 and n_2 are the maximum and minimum porosities, respectively, p is the pressure, Δ is the arithmetic width of the transition from high porosity to low porosity ($0.33\text{--}0.58$ depending on the compression style), and p_m is the turnover pressure. If no additional load is added onto the lunar surface, the pressure in lunar regolith should be dominated by hydrostatic pressure. In addition, as the hydrostatic pressure within lunar regolith relies on the depth following the expression

$$p(z) = \int_0^z \rho(\text{FeO}, \text{TiO}_2, z') g dz' \quad (6)$$

where g is the gravitational acceleration, the porosity transition within lunar regolith is essentially caused by the variation of hydrostatic pressure versus depth. Correspondingly, the maximum and minimum porosities in Eq. (5) should be equal to n_s and n_d respectively.

Because the H factor in Eq. (3) controls the rate of porosity increase in the near-surface layer, the physical meaning of this parameter can be derived from the two equations above. In order to extract hydrostatic pressure from Eq. (5), we inverse this equation to the following form

$$p(n) = p_m \left(\frac{n_s - n_d}{n - n_d} - 1 \right)^{\Delta \ln 10} \quad (7)$$

The H factor in Eq. (3) represents the depth at which the porosity increases to $(0.63n_s + 0.37n_d)$. We determine the hydrostatic pressure at the depth of H factor from Eqs. (6) and (7), which yields the expression to determine H factor

$$H(r, g, G) = p_m \frac{0.58^{\Delta \ln 10}}{gG(0.37n_d + 0.63n_s)} \quad (8)$$

Under the assumption of the independence between Δ and grain radius, the turnover pressure can be obtained from the expression (Schräpler et al., 2015)

$$p_m(r) = F_0(1 - n_1)r_0^{-2/3}\pi^{-1}r^{-4/3} \quad (9)$$

where F_0 is a material parameter, r_0 is the reference radius, and r is the grain radius.

The specific heat capacity of lunar regolith (unit: $\text{J kg}^{-1} \text{K}^{-1}$) can be expressed as a function of temperature (Keihm, 1984)

$$C(T) = 670 + 10^3 \left(\frac{T-250}{530.6} \right) - 10^3 \left(\frac{T-250}{498.7} \right)^2 \quad (10)$$

Note that this equation is applicable to global lunar regolith because the specific heat capacity of lunar regolith varies insignificantly from sample to sample (Robie et al., 1970; Hemingway et al., 1973).

The thermal conductivity of lunar regolith is composed of solid thermal conductivity and radiative thermal conductivity, which can be expressed as (Presley and Christensen, 1997)

$$K(z, T) = K_c(z) + BT^3 \quad (11)$$

where $K_c(z)$ is solid thermal conductivity, B is a coefficient contained in radiation conductivity. Assuming that the planetary regolith is composed of the closely packed grains in the same size, Gundlach and Blum (2013) determine the solid thermal conductivity as the following expression

$$K_c(r, T, n) = K_0 \cdot \left[\frac{9\pi}{4} \frac{1-\mu^2}{E} \frac{\gamma(T)}{r} \right]^{1/3} \cdot [f_1 e^{f_2(1-n)}] \cdot \kappa \quad (12)$$

where K_0 is the thermal conductivity of solid grains, μ is Poisson's ratio, E is Young's modulus, $\gamma(T)$ is the specific surface energy, f_1 and f_2 are two empirical coefficients calibrated as $(5.18 \pm 3.45) \times 10^{-2}$ and 5.26 ± 0.94 , respectively, and κ is a correction factor (0.41 ± 0.02) for the irregular shape of regolith grains. Note that specific surface energy is actually a function of temperature. Because the solid thermal conductivity of lunar regolith relies on porosity, the solid thermal conductivity should be a function of depth. In order to simplify the profile of solid thermal conductivity, we adopt the following expression (Vasavada et al., 2012; Hayne et al., 2013) as an approximation of Eq. (12)

$$K_c(z) = K_d - (K_d - K_s) \exp(-z/H) \quad (13)$$

where K_d and K_s are the solid thermal conductivity on the surface and at subsurface respectively. These two parameters can be determined from the following two expressions

$$K_s = K_0 \cdot \left[\frac{9\pi}{4} \frac{1-\mu^2}{E} \frac{\gamma(T)}{r} \right]^{1/3} \cdot [f_1 e^{f_2(1-n_s)}] \cdot \kappa \quad (14)$$

$$K_d = K_0 \cdot \left[\frac{9\pi}{4} \frac{1-\mu^2}{E} \frac{\gamma(T)}{r} \right]^{1/3} \cdot [f_1 e^{f_2(1-n_d)}] \cdot \kappa \quad (15)$$

In the regime of $H \leq 0.20$ m, this approximation can only produce a relative error of about 3% on average with respect to Eq. (12). Note that this relative error is determined by averaging the non-zero relative errors at all the depths.

The coefficient B was assumed to be a constant $3.78 \times 10^{-11} \text{ W m}^{-1} \text{ K}^{-4}$ in the previous investigations (Keihm, 1984; Miyahara et al., 2008; Grott et al., 2010). Gundlach and Blum (2013) determine this coefficient as the following expression

$$B(n, r) = 8\sigma\epsilon\Lambda(n, r) \quad (16)$$

where σ is the Stefan-Boltzman constant ($5.67 \times 10^{-8} \text{ W m}^{-2} \text{ K}^{-4}$), ϵ is the emissivity of lunar regolith grains (assumed to be unity), $\Lambda(n, r)$ is the mean free path of photons that can be determined from

$$\Lambda(n, r) = e_1 \frac{n}{1-n} r \quad (17)$$

where e_1 is an empirical coefficient (1.41 ± 0.01). Given the average grain radius $30 \mu\text{m}$ and the typical porosity range $0.38-0.58$, this coefficient varies from 1.17×10^{-11} to $2.65 \times 10^{-11} \text{ W m}^{-1} \text{ K}^{-4}$.

Table 1

The typical values of lunar regolith's thermophysical parameters.

Parameter	Typical value	Unit	Reference
n_s	0.58 ± 0.02	–	Carrier et al. (1991)
n_d	0.38 ± 0.02	–	Carrier et al. (1991)
r	30 ± 10	μm	–
H	0.06 ± 0.04	m	Vasavada et al. (2012)
K_s	0.0006 ± 0.0003	$\text{W m}^{-1} \text{ K}^{-1}$	Vasavada et al. (2012)
K_d	0.007 ± 0.0003	$\text{W m}^{-1} \text{ K}^{-1}$	Vasavada et al. (2012)

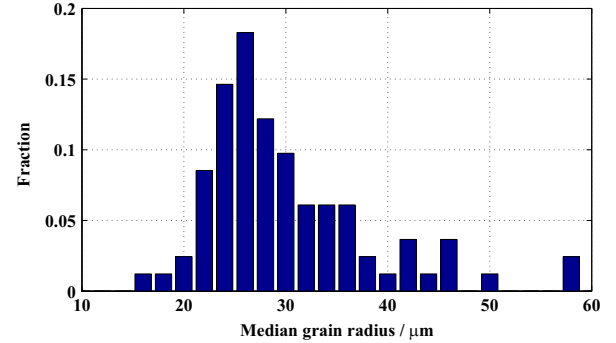


Fig. 1. The histogram of median grain radius for the regolith samples returned from Apollo 17 landing site. The data are obtained from Table 9.2A in Carrier et al. (1991).

Therefore, the coefficient B cannot be fixed as a constant and Eq. (16) is adopted to determine this coefficient in this study.

Till now, the distributions of these thermophysical parameters are still poorly known apart from those laboratory or in-situ experiment data for the samples returned from Apollo landing sites. It is uncertain whether these data could represent the conditions of global lunar regolith or not. In order to test the feasibility of our estimation, the typical values of these parameters should be realized at first from those previous investigations on Apollo samples.

Table 1 shows the typical values of these thermophysical parameters determined from the data and theories in the previous investigations. The knowledge about the bulk density of lunar regolith mainly originates from the laboratory experiments on the core drilling samples returned in Apollo missions. Carrier et al. (1991) give the best fitted expression for these data in which the bulk density of lunar regolith is about 1300 kg m^{-3} on the surface, increases rapidly within tens of centimeter atop and converges on 1920 kg m^{-3} at subsurface. Given a typical G value 3100 kg m^{-3} , the typical porosities of surface and subsurface lunar regolith can be determined as 0.58 and 0.38 respectively. The uncertainty of porosities are specified as ± 0.02 shown in this work. Note that the porosity of lunar regolith still lacks in accurate constraint. In this study, we assume that the porosity of lunar regolith does not vary laterally.

The knowledge about the size of lunar regolith grains mainly derives from those experiment data for Apollo 17 regolith samples. Because the global distribution of this parameter is still unknown, we adopt the median grain radius data for the regolith samples returned from this landing site as an alternative choice (see Table 9.2A in Carrier et al., 1991). These median radius data take an average value of about $30 \mu\text{m}$. In addition, as shown in Fig. 1, more than 90% median grain radius data fall between 20 and $40 \mu\text{m}$. According to this statistic result, we specify $30 \pm 10 \mu\text{m}$ as the typical value of grain radius.

Based on Diviner channel-7 data at lunar equator, Vasavada et al. (2012) estimate the typical values of K_s , H and K_d as $0.0006 \text{ W m}^{-1} \text{ K}^{-1}$, 0.06 m and $0.007 \text{ W m}^{-1} \text{ K}^{-1}$ respectively. We adopt these results to represent the typical values of these

three parameters. However, it needs to clarify that the estimations in Vasavada et al. (2012) just represent the average condition at lunar equator. Except those data collected at several Apollo landing sites, the global distributions of these three parameters are still unknown. As an alternative choice, we have to determine their uncertainties following the laboratory experiment data as well as other theoretical analysis. The laboratory experiments for Apollo returned samples yield the K_s values ranging from $0.0005 \text{ W m}^{-1} \text{ K}^{-1}$ to $0.0009 \text{ W m}^{-1} \text{ K}^{-1}$ (Cremers and Birkebak, 1971; Cremers and Hsia, 1974). Here we neglect the experiment result for the regolith sample from Apollo 11 landing site because these data are not complete to analyze the temperature dependence of thermal conductivity. Therefore, the typical value of K_s can be specified as $0.0006 \pm 0.0003 \text{ W m}^{-1} \text{ K}^{-1}$.

The typical value of H factor was poorly constrained in the past. Hayne et al. (2013) estimate the H factor in three mare regions from Diviner rock-free temperature by fixing the value of K_s as $9.22 \times 10^{-4} \text{ W m}^{-1} \text{ K}^{-1}$. However, because K_s would also vary laterally, the estimated H factor therein would also couple the effect of K_s variation. So the typical value of H factor should be given in other manner. In Eq. (8), we have indicated that the H factor can be expressed as a function of grain radius, density of solid grains, the arithmetic transitional width, gravitational acceleration and porosity. Here we will try to derive the uncertainty of H factor by using this equation. Assuming that lunar regolith only undergoes an omnidirectional compression induced by hydrostatic pressure, the arithmetic transitional width should keep constant across the entire lunar surface. In this case, the H factor can be approximated by using a scaling relation

$$H(r, G, g) = H_0 \left(\frac{r}{r_0} \right)^{-3/4} \left(\frac{G}{G_0} \right)^{-1} \left(\frac{g}{g_0} \right)^{-1} \quad (18)$$

where H_0 is the H factor value at the typical grain radius (r_0), density of solid grains (G_0) and gravitational acceleration (g_0). Because the estimation in Vasavada et al. (2012) represents the average condition at lunar equator, it would be safe to assume that 0.06 m represents the H factor at the typical grain radius and density of solid grains. As the discussions above, we assume that the typical grain radius and density of solid grains are $30 \mu\text{m}$ and 3100 kg m^{-3} , respectively. Given the typical ranges of grain radius ($20\text{--}40 \mu\text{m}$) and density of solid grains ($2900\text{--}3800 \text{ kg m}^{-3}$ calculated from the iron and titanium abundances in Lunar Prospector gamma-ray spectrum data), the typical range of H factor can be determined as $0.03\text{--}0.10 \text{ m}$. On the basis of this calculation, we specify the typical value of H factor as $0.06 \pm 0.04 \text{ m}$.

The average K_d value at lunar equator is prominently lower than the value $0.0093 \text{ W m}^{-1} \text{ K}^{-1}$ obtained from Apollo heat flux experiments (Langseth et al., 1976). It needs to caution that the temperature probe is able to compact surrounding lunar regolith and lead to a prominent increase of subsurface solid thermal conductivity. Grott et al. (2010) indicate that this compaction is able to increase the estimated K_d value by about $0.0020 \text{ W m}^{-1} \text{ K}^{-1}$, which implies that the probed K_d value without compaction should be around $0.0073 \text{ W m}^{-1} \text{ K}^{-1}$. In addition, the corrected subsurface solid thermal conductivity is basically consistent with the estimation in Vasavada et al. (2012). Therefore, $0.0070 \text{ W m}^{-1} \text{ K}^{-1}$ can be used as the typical value of K_d . Correspondingly, we specify the uncertainty of K_d as $\pm 0.0003 \text{ W m}^{-1} \text{ K}^{-1}$, which represents the difference between the estimation in Vasavada et al. (2012) and the corrected K_d value in Grott et al. (2010).

2.2. Temperature model

Heat conductive equation is adopted to correlate lunar surface temperature with the thermophysical properties of lunar regolith

$$\rho C \frac{\partial T}{\partial t} = \frac{\partial}{\partial z} \left(K \frac{\partial T}{\partial z} \right) \quad (19)$$

The perturbations of solar insolation and heat flow can be incorporated into Eq. (19) through the boundary conditions on the surface and at subsurface

$$K(z, T) \frac{\partial T}{\partial z} \Big|_{z=0} = TSI(1-A) \cos^+ i - e\sigma T_s^4 - J_0 \quad (20)$$

$$K(z, T) \frac{\partial T}{\partial z} \Big|_{z=-\infty} = -J_0 \quad (21)$$

where TSI is the solar irradiance at 1 AU, A is the surface albedo, e is the broadband emissivity of lunar surface, i is solar incident angle, T_s is the temperature of lunar surface, and J_0 is the heat flow on the surface. The symbol $\cos^+ i$ is equal to $\cos i$ if $i \leq 90^\circ$ and zero otherwise. Because this study only focuses on lunar surface temperature, the heat flow can be assumed to be zero due to its small effect on surface temperature.

The lunar surface can be modelled as a non-Lambertian surface whose albedo relies on solar incident angle. We adopt the following empirical expression to determine the albedo of lunar surface (Keihm, 1984)

$$A(i) = A_0 + a \left(\frac{i}{\pi/4} \right)^3 + b \left(\frac{i}{\pi/2} \right)^8 \quad (22)$$

where A_0 is the normalized albedo (0.07 and 0.16 for mare and highland respectively), a and b are two empirical coefficients estimated as 0.045 and 0.14 respectively from Diviner observations on lunar equator (Vasavada et al., 2012). Given that the geometric relation between the Sun and local topographic cell is shown in Fig. 2, the solar incident angle can be determined from the expression

$$i = \cos^{-1} [\cos \theta_p \cos Z_s + \sin \theta_p \sin Z_s \cos (A_s - \phi_p)] \quad (23)$$

where θ_p is the slope angle, ϕ_p is the aspect angle, Z_s is the solar zenith angle, and A_s is the solar azimuth angle. The solar zenith angle and azimuth angle relies on the geometric relation between the Sun and the Moon and can be predicted from

$$Z_s = \cos^{-1} [\cos \lambda \cdot \cos (t \times \pi/12 - \pi)] \quad (24)$$

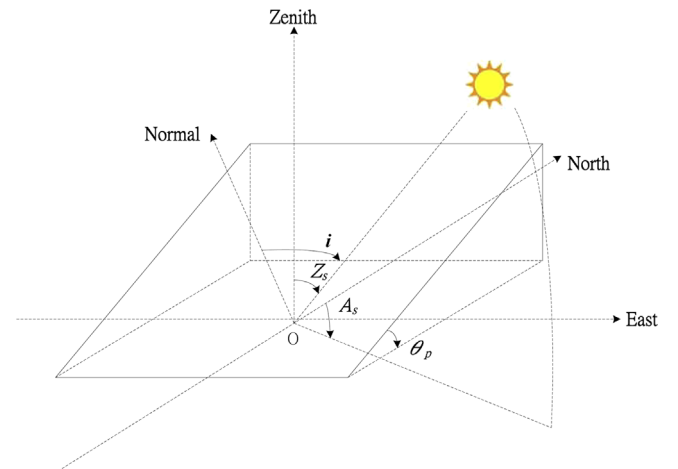


Fig. 2. The geometric relation between the Sun and local topography.

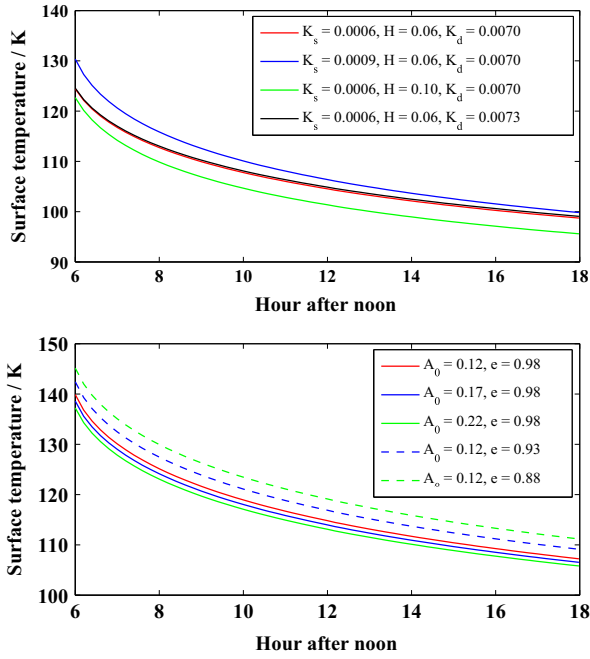


Fig. 3. The sensitivity of nighttime surface temperature to the variations of K_s , H factor, K_d (upper), surface albedo and surface emissivity (lower). Except the specified ones, other parameters are fixed as their typical values (i.e. $\lambda=0^\circ$, $A_0=0.12$, $e=0.98$, $\text{FeO}=5$ wt%, $\text{TiO}_2=1$ wt%, $\theta_p=0^\circ$, $\phi_p=0^\circ$ and the typical values are shown in Table 1).

$$A_s = \cos^{-1} \left[\frac{\cos(t \times \pi/12 - \pi) \cdot \sin \lambda}{\cos(\pi/2 - Z_s)} \right] \quad (25)$$

where λ is the latitude and t is the local time on the Moon. Note that the inclination angle of the Moon is neglected in these two equations.

2.3. Sensitivity tests

In this section, we will test the sensitivity of nighttime surface temperature to the parameters used in our temperature model. As the prerequisite of K_s estimation, the K_s variation should have a prominent influence on the surface temperature. At the same time, the analysis of estimation error also requires to know the effects of other parameters on the surface temperature in advance.

Fig. 3 shows the nighttime surface temperature variations obtained by inputting different sets of parameters to the temperature model. Except the specified ones, the parameters are fixed to their typical values (i.e. $\lambda=0^\circ$, $A_0=0.12$, $e=0.98$, $\text{FeO}=5$ wt%, $\text{TiO}_2=1$ wt%, $\theta_p=0^\circ$, $\phi_p=0^\circ$ and the typical values shown in Table 1). Here we do not consider the effects of FeO and TiO_2 abundances because these two parameters can be read from the data of Lunar Prospector gamma-ray spectrum or Clementine UVVIS spectroscopy (Lucey et al., 1995; Prettyman et al., 2006). As seen from Fig. 3 (upper), the K_s value dominates the whole level of surface temperature and a $0.0003 \text{ W m}^{-1} \text{ K}^{-1}$ variation of this parameter (i.e. 50% variation with respect to the typical value of K_s) can perturb the surface temperature by about 3 K. The H factor mainly affects the decrease rate of surface temperature. In case of larger H factor, the surface temperature decreases more rapidly within the first two hours after sunset, which leads to a lower temperature in the latter period. Quantitatively, a 0.04 m variation of H factor (i.e. 66.7% variation with respect to the typical value of H factor) can affect the temperature curve by about 2 K. It needs to be cautioned that both K_s and H factor can affect the whole level of surface temperature prominently and their effects would be highly

coupled in Diviner observations. In Section 3, we will discuss more details about this problem.

The subsurface solid thermal conductivity K_d does not have prominent influence on the surface temperature. As shown in Fig. 3 (upper), a $\pm 0.0003 \text{ W m}^{-1} \text{ K}^{-1}$ variation of K_d (i.e. about 4.3% variation with respect to the typical value of K_d) can perturb the surface temperature by about 0.2 K. As the uncertainty of this parameter is specified as $\pm 0.0003 \text{ W m}^{-1} \text{ K}^{-1}$, this uncertainty range cannot affect the nighttime surface temperature prominently. So it would be secure to set this parameter to a constant in the estimation.

In addition, we also test the influences of surface albedo and emissivity on the surface temperature. As shown in Fig. 3 (lower), both these two parameters only affect the whole level of surface temperature. The decrease of these two parameters can elevate the whole level of nighttime surface temperature. So the influences of these two parameters cannot be neglected in the estimation. In Section 3, we will discuss more details about this problem.

2.4. Lateral heat conduction

Eq. (19) only considers the heat conduction in the vertical direction, so the simulated surface temperature actually represents the condition without lateral heat flux. In fact, lunar surface temperature also has a lateral variation dominated by local time and latitude. Assuming that the local time at the longitude 0° is 12:00, the distribution of surface temperature between 60°N and 60°S are calculated by using our temperature model and shown in Fig. 4 (upper). Here the spatial resolution is fixed to 1° (about 30 km on the lunar surface) and the thermophysical parameters are fixed to their typical values and do not vary laterally. The topographic fluctuation is neglected in order to enhance the effects of local time and latitude on the surface temperature. As seen from this simulation result, the lateral variation of surface temperature is very drastic, so the influence of lateral heat conduction has to be cautioned.

If the lateral heat flux calculated from the simulated surface temperature was far smaller than the vertical heat flux, the simulated surface temperature should be valid. Fig. 4 (middle) shows the lateral heat flux calculated from the simulated surface temperature. As seen from this figure, the highest lateral heat flux appears near the terminator (about $3 \times 10^{-7} \text{ W m}^{-2}$ on average). The lateral heat flux in the nighttime regime is at the level of about 10^{-9} W m^{-2} , whereas the lateral heat flux in the daytime regime varies in a wide range between 10^{-9} and 10^{-7} W m^{-2} . In addition, the vertical heat flux on the lunar surface is also calculated and shown in Fig. 4 (lower). As read from this figure, the vertical heat flux varies between 10 and 75 W m^{-2} in the daytime regime, whereas it varies between 4 and 21 W m^{-2} in the nighttime regime. Therefore, the surface temperature of the Moon can be well sketched by the heat conductive equation in one dimension.

3. Estimation strategy

3.1. Dataset

Diviner is a high-resolution radiometer on Lunar Reconnaissance Orbiter (LRO) that aims to observe the thermal condition of lunar surface through four TIR channels (Paige et al., 2010). Now the data products of Diviner radiometer are archived and open to public in Planetary Data System (PDS) geosciences node. Our estimation is carried out based upon Level-3 bolometric temperature dataset generated from the nadir observations obtained between 2009 and 2011. Because this study focuses on the

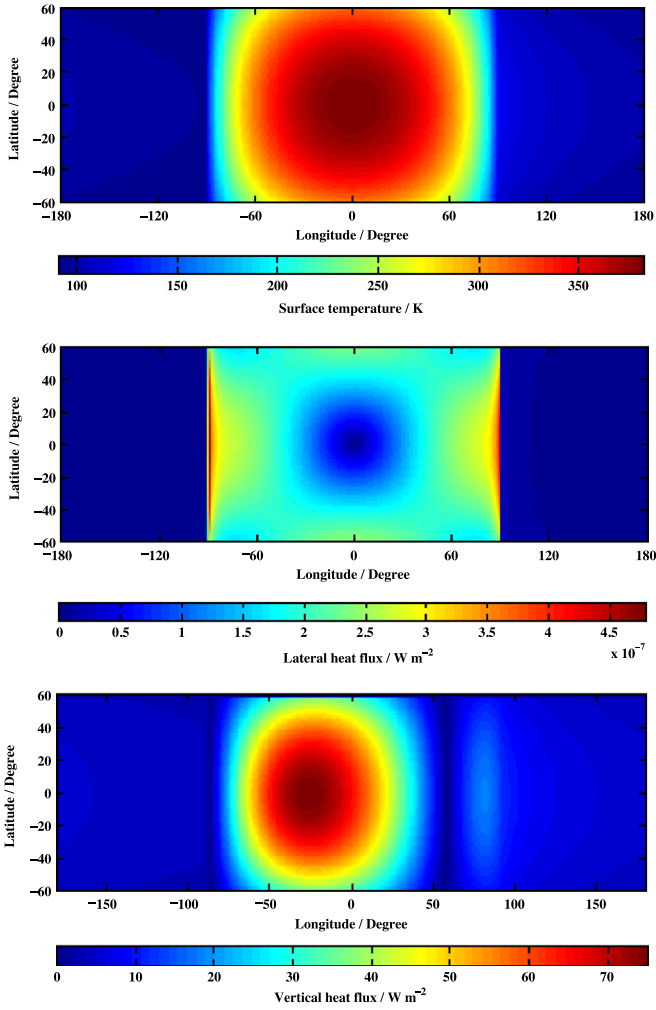


Fig. 4. The upper figure shows the distribution of surface temperature obtained from Eq. (19) by assuming the local time at the longitude 0° as 12:00. The middle figure shows the lateral heat flux calculated from the surface temperature shown in the upper figure. The lower figure shows the vertical heat flux on the lunar surface.

distribution of solid thermal conductivity throughout the entire lunar surface, the gridded data products with one record per degree are adopted. The local time information is stored in Level-2 local time image (LTIM) files. For more information about Diviner dataset, readers can refer to the materials of data processing in Williams et al. (2015).

Per definition, bolometric temperature is the temperature of a blackbody that emits the same integrated radiation flux. Unless the lunar surface is an isothermal blackbody, bolometric temperature is not strictly equivalent to the surface temperature of the Moon. Actually, the temperature of lunar surface has a complex distribution dominated by rock abundance and the topographic fluctuation at all spatial scales. So these two factors should be cautioned in the analysis of bolometric temperature data.

In previous investigations, the influences of rock debris on Diviner observations have been studied in detail. Because rock debris has higher thermal inertia, the protruding or partially buried boulders in the size larger than skin depth (about 50 cm on the Moon) behave as the major high temperature anomalies on the lunar surface. Due to the non-uniformity of blackbody radiance spectrum, the Diviner observations in different channels possess different sensitivities to these temperature anomalies, which leads to the anisothermality across the wavelength. The observations in short wavelength channels are more sensitive to the temperature anomalies on the lunar surface, whereas the observations in long

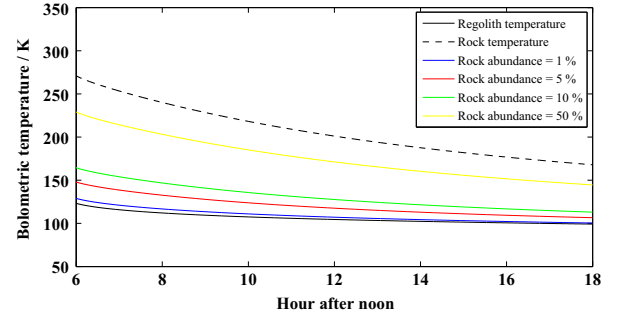


Fig. 5. The bolometric temperature curves with different rock abundances obtained from simulation. The increase of rock abundance can elevate the whole level of bolometric temperature substantially.

wavelength channels are more sensitive to the scene average of all the radiative contributions within the field of view (FOV). Based upon this principle, Bandfield et al. (2011) estimate the rock abundance on the lunar surface from the anisothermality at short wavelength.

Because bolometric temperature is a measure of total radiation flux, this quantity should be sensitive to the average of all the temperature contributions within the FOV. As the consequence, the radiative contributions from those protruding or partially buried boulders are smeared across the entire radiance spectrum and elevate the whole level of bolometric temperature throughout the lunar night. If the material on the lunar surface is only composed of boulders and regolith fine, the bolometric temperature can be determined from

$$T_{bol}(t) = \left[(1 - R_A) e T_s^4(t) + R_A e_r T_r^4(t) \right]^{1/4} \quad (26)$$

where R_A is the rock abundance, e_r is the emissivity of rock debris, and T_r is the temperature of rock debris. In this study, we assume that the emissivity of rock debris is identical to the emissivity of lunar surface.

The nighttime bolometric temperature curves with different rock abundances are calculated and shown in Fig. 5. Here the rock temperature is simulated by assuming the density and thermal conductivity within skin depth to be 3100 kg m^{-3} and $1.5 \text{ W m}^{-1} \text{ K}^{-1}$ respectively, while the thermophysical properties of lunar regolith, surface albedo, surface emissivity and solar insulation parameters are fixed to their typical values (i.e. $\lambda=0^\circ$, $A_0=0.12$, $e=0.98$, $\text{FeO}=5 \text{ wt\%}$, $\text{TiO}_2=1 \text{ wt\%}$ and the values shown in Table 1). The slope angle θ_p and slope aspect ϕ_p are set to zero. As seen from this figure, the increase of rock abundance can elevate the whole level of bolometric temperature curve prominently. In fact, rock debris is not a major barrier in carrying out the estimation of K_s from bolometric temperature dataset. The estimation in Bandfield et al. (2011) shows that the rock abundance in most area of lunar surface is far less than 1%. Therefore, bolometric temperature can behave as a good proxy of lunar surface temperature. In Section 3.7, we will discuss more details about the influence of rock abundance on the estimated K_s .

The topographic fluctuation also affects the observed bolometric temperature in a similar manner. For example, the equator facing slope will retain a higher temperature throughout the lunar night, whereas the equator dorsal slope will persist a lower temperature throughout the lunar night. As topographic fluctuation cannot be avoided, those regions without rock debris is still not strictly isothermal. Bandfield et al. (2015) estimate the influences of topographic fluctuation on the nadir observed TIR brightness temperatures at different wavelengths, which shows that topographic fluctuation can result in a prominent anisothermality not only across the spectrum of brightness temperature but also versus the emission angle. In addition, we have to emphasize that the

topographic fluctuation on the Moon also possesses different characteristics at different scales (Rosenburg et al., 2011; Cao et al., 2015) and this effect was not considered in the roughness model adopted in Bandfield et al. (2015). Consequently, topographic fluctuation should have a complicated influence on the observed bolometric temperature that relies on not only the drastic degree of fluctuation but spatial scale as well. Even though our temperature model has coupled slope angle and slope aspect, this improvement cannot reflect the roughness at different scales. Due to this reason, we will not consider the effects of topographic fluctuation in our estimation.

On the other hand, the shadowing effect caused by topography would become very prominent in the high latitude region. In an extreme case, some craters in lunar polar regions are permanently shaded and their temperatures keep an extremely low level during much of lunar history. Our temperature cannot be handled with this condition very well. To avoid this problem, we consider the region between 60°N and 60°S in the estimation.

3.2. Method

As the implications of temperature model, lunar surface temperature is actually a function of latitude, surface albedo, emissivity, the thermophysical properties of lunar regolith and topography. If the parameters other than K_s were known, the estimation is essentially an inversion problem from multiple observations to one parameter in an over-determined system. Therefore, the solution can be obtained by a least-square method that searches for the optimal K_s when the minimum deviation between Diviner observations and the simulated surface temperature is achieved. The deviation can be quantified as the root-mean-square error (RMSE) between them

$$\Delta T_{RMS} = \sqrt{\frac{\sum_i [T_m(t_i) - T_o(t_i)]^2}{N}} \quad (27)$$

where ΔT_{RMS} is RMSE, $T_m(t_i)$ is the simulated temperature at i th local time, $T_o(t_i)$ is the observation at i -th local time, and N is the total number of observations.

In the following sections, we will discuss the potential estimation error originating from observation error, the data coverage along local time and the uncertainties of parameters. The former two factors depend on the in-orbit performances of radiometer as well as the orbital coverage, which cannot be controlled in the estimation. So their influences are required to be quantified priorly. On the other hand, the parameters other than K_s require to be fixed in the estimation. The slope angle θ_p and slope aspect ϕ_p are set to zero all the time. Other parameters such as surface and subsurface porosities, H factor and subsurface solid component were poorly constrained in the past. An alternative choice is to set these parameters into their typical values, but the influences of their uncertainties also require to know in advance.

3.3. Why estimates K_s ?

As shown in Fig. 3, both K_s and H factor can affect the whole level of lunar surface temperature prominently and their effects are highly coupled. In principle, estimating these two parameters simultaneously should be a better option to decouple their effects from Diviner data. However, we need to emphasize the difficulties in performing the least-square fitting with multiple free parameters. Because the surface temperature is calculated numerically, the analytical solution to the RMSE cannot be given. As an alternative choice, Nelder–Mead algorithm (i.e. a dimensionless simplex search method) is adopted to seek the minimum RMSE between Diviner observations and the simulated surface

temperature (Nelder and Mead, 1965). Essentially, this algorithm aims to find the minimum RMSE by shrinking the search domain iteratively. However, the convergence of this algorithm is still an open question in computer sciences. Till now, the convergence of the simplex search with more than two free parameters is still not comprehensively understood (Lagarias et al., 1998). In fact, the simplex search with multiple free parameters is more common to diverge in our diagnostic tests. On the other hand, the efficiency of Nelder–Mead algorithm also relies on the number of free parameters. Our diagnostic tests show that the time of the simplex search with more than two free parameters is at least 5–7 times longer than the simplex search with single free parameter. At writing this paper, we have not found any good solutions to this problem.

As the least-square fitting only allows single free parameter, it is necessary to clarify the reasons why K_s is selected as the estimation target. The major reason is concerned with the information about the intrinsic properties of lunar regolith contained in these two parameters. In Section 2.1, we have shown that these two parameters can be expressed as the functions of the intrinsic properties of lunar regolith. Except porosity and the intrinsic properties of solid grains, H factor only relies on grain radius, whereas K_s relies on grain radius and specific surface energy. Therefore, K_s contains more information about the intrinsic properties of lunar regolith.

In addition, as K_s and H factor correlate with grain radius and specific surface energy inherently, estimating grain radius is an alternative choice to decouple the effects of K_s and H factor from Diviner observations. However, because specific surface energy also relies on temperature, the surface temperature simulation also requires to know the relation between these two parameters in advance. But till now, there is still no reliable theory to quantify this relation. Some investigations also try to derive the empirical relation between specific surface energy and temperature. Intuitively, the increase of temperature is able to increase the rate of dipoles per molecule, so specific surface energy should increase with temperature monotonically. Based upon this principle, Gundlach and Blum (2012) derive an empirical expression to determine specific surface energy (unit: J m⁻²) from temperature

$$\gamma(T) = 6.67 \times 10^{-5} T \quad (28)$$

Note that this equation is obtained by a linear interpolation between the assumed zero surface energy at 0 K and the experimental value 0.02 J m⁻² at 273 K for spherical glasses. Because the linearity between specific surface energy and temperature has no physical basis, we hold a conservative attitude towards the reliability of Eq. (28).

3.4. Correctness and quality of fitting

In order to verify the correctness of our estimation strategy, we perform the estimation to the bolometric temperature data at lunar equator (i.e. within the latitude $0 \pm 0.5^\circ$). As shown in Fig. 6, our estimation strategy yields the best fitted K_s value 0.0009 W m⁻¹ K⁻¹, which is slightly higher than the best fitted K_s value 0.0006 W m⁻¹ K⁻¹ obtained in Vasavada et al. (2012). It is necessary to note that the difference between these two estimations is essentially caused by the different thermal conductivity profiles used in individual fitting strategies. In Vasavada et al. (2012), the thermal conductivity of lunar regolith is determined from the expression

$$K_{vas,2012}(z, T) = K_c(z)[1 + \chi(T/350)^3] \quad (29)$$

where χ is an empirical coefficient (equal to 2.7) representing the ratio between solid thermal conductivity and the radiative solid conductivity at 350 K. In fact, the correlation between radiative

part and porosity in Eq. (29) is highly simplified to the product between solid thermal conductivity and an empirical coefficient. As this simplification does not have consolidated physical basis, our best-fit K_s value should be more reliable.

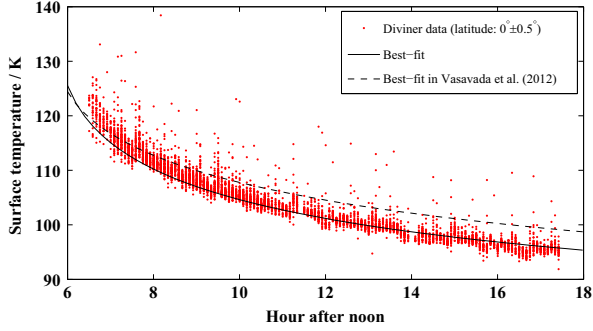


Fig. 6. The Diviner bolometric data at lunar equator (latitude: $0 \pm 0.5^\circ$) are selected to test the fitting quality. Our least-square fitting yields the best fitted K_s value $0.0009 \text{ W m}^{-1} \text{ K}^{-1}$, which is basically consistent with the K_s value $0.0006 \text{ W m}^{-1} \text{ K}^{-1}$ obtained in Vasavada et al. (2012).

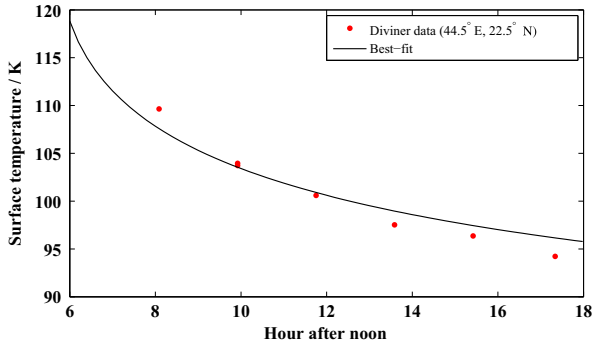


Fig. 7. The data at 44.5°E , 22.5°N are selected as the example to test the quality of least-square fitting.

The bolometric temperature data at 44.5°E , 22.5°N are selected as the example to test the quality of least-square fitting. As shown in Fig. 7, the bolometric temperature variation can be well sketched by the best fitted curve yielded from our estimation strategy.

3.5. Test on observations

A Monte-Carlo simulation is performed to test the sensitivity of estimation error to the observation error and the data coverage along local time. As *a priori* knowledge, the typical nighttime surface temperature is determined at first by inputting the parameter values $\lambda=0^\circ$, $A_0=0.12$, $e=0.98$, $\text{FeO}=5 \text{ wt\%}$, $\text{TiO}_2=1 \text{ wt\%}$, $\theta_p=0^\circ$, $\phi_p=0^\circ$ and the typical values shown in Table 1 to the temperature model. The observations can be generated by incorporating a random noise ΔT_o into the simulated temperatures sampled at N random time points. The random noise is assumed to obey a normal distribution $N(0, \sigma_o)$ where σ_o is the standard deviation of observation error. In this case, a K_s value can be estimated from the generated observations through the estimation strategy above and a relative estimation error with respect to the typical K_s value (noted as $\Delta K_s/K_s$) is also able to be determined. The random experiment is repeated for 200 times and the obtained relative errors are also averaged versus experiment number.

Fig. 8 shows the average relative error ($\Delta K_s/K_s$) as the function of observation number and standard deviation of observation error. In all the simulations, the average estimation error tends to converge after about 100 experiments. As seen from the experiment results, the average estimation error can be reduced by increasing the observation number and specially, it tends to be stable if more than 8 observations are used. Actually, it means that the estimation error induced by the data coverage along local time has been reduced substantially and the residual error is only caused by observation error. On the other hand, it is clear that the estimation error also increases proportionally to the standard deviation of observation error. For example, given an observation

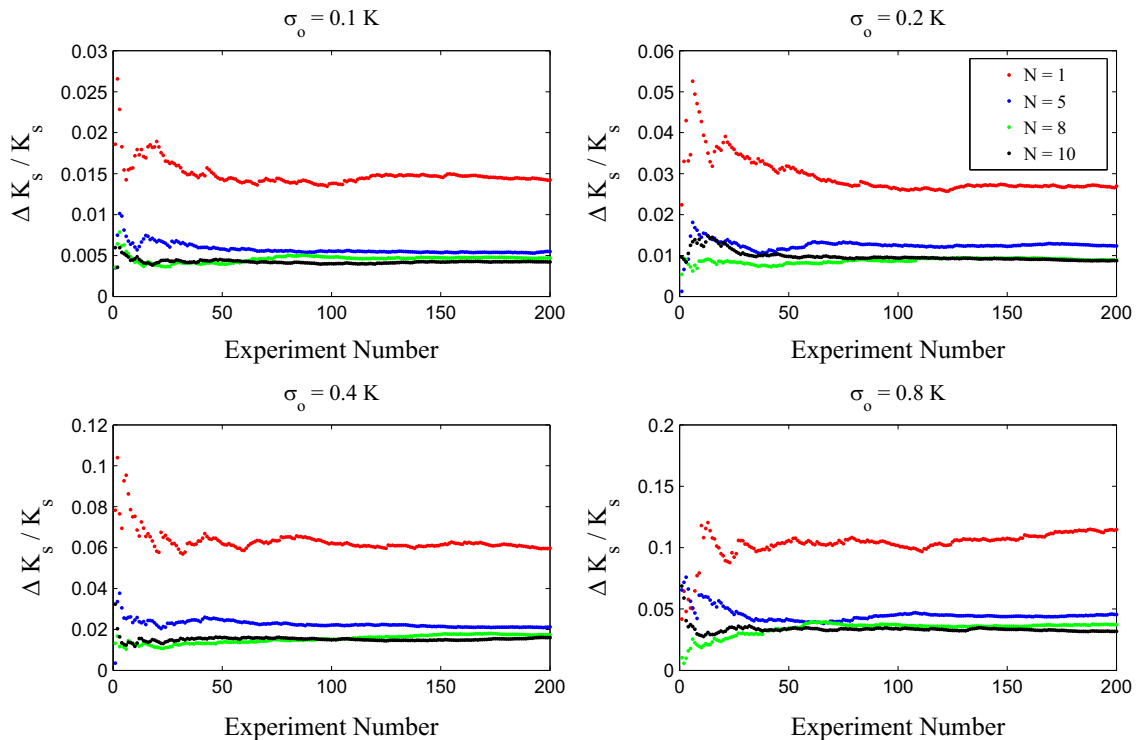


Fig. 8. The sensitivity of relative estimation error ($\Delta K_s/K_s$) to the number of observations (N) and the standard deviation of observation error (σ_o) obtained from Monte-Carlo simulations.

number 10, the estimation errors at the standard deviations of observation error 0.1, 0.2, 0.4 and 0.8 K are calculated as about 0.5%, 1.0%, 2.0% and 4.0% respectively.

We also count the number of Diviner data records in every $1^\circ \times 1^\circ$ cells between 60°N and 60°S . As shown in Fig. 9, more than 85% cells on the lunar surface are covered by 8–10 data records at different local time, while most of the remaining cells are covered by at least 6 data records at different local time. Only a minor fraction of cells are covered by less than 6 data records. The counting result indicates that the estimation error induced by observation number can be neglected in most area of lunar surface. However, because the potential observation error is not provided in the Diviner dataset, the estimation error induced by this factor cannot be constrained quantitatively.

3.6. Test on parameter uncertainties

In order to quantify the relations between estimation error and the uncertainties of those parameters with fixed values, we determine the K_s from the observations generated by inputting the offsetted parameters to the temperature model and then, calculate its relative error with respect to the typical value of K_s shown in Table 1. To avoid the perturbation of observation number, the simulated temperature curve is sampled with an interval of 0.02 h

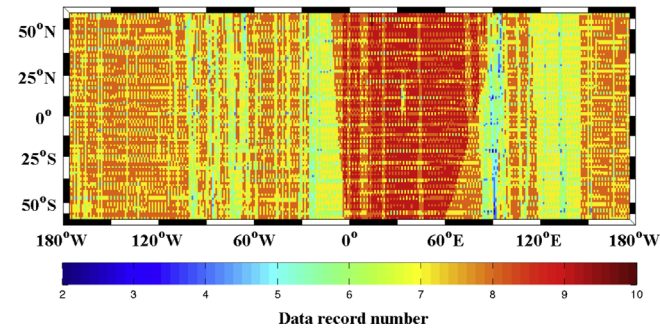


Fig. 9. The data record number in every $1^\circ \times 1^\circ$ cells between 60°N and 60°S throughout lunar night.

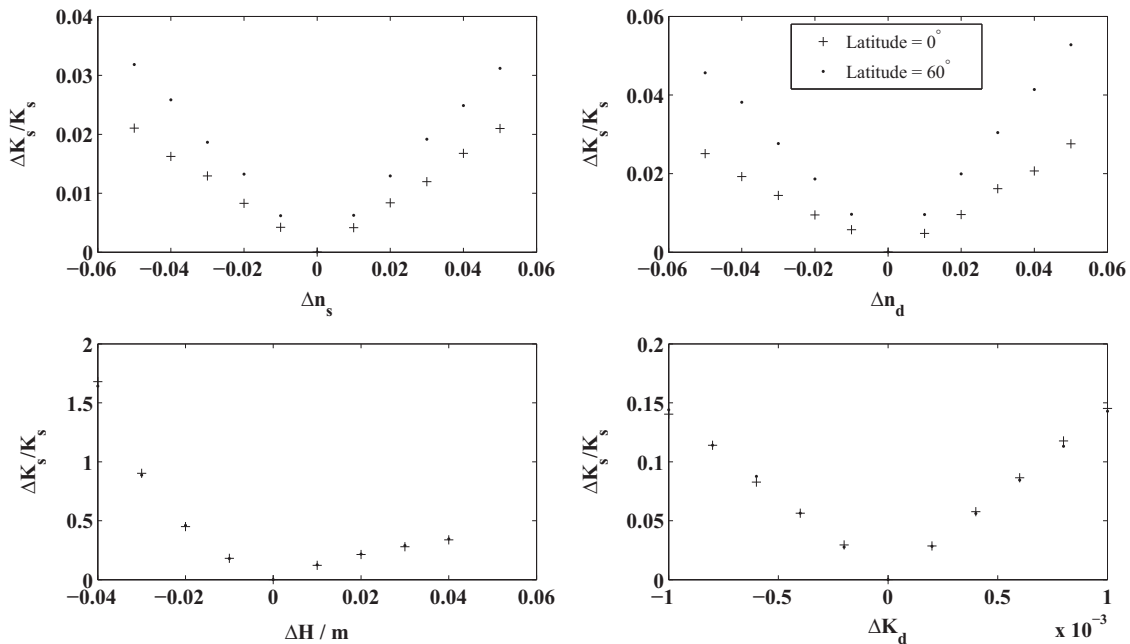


Fig. 10. The sensitivity of estimation error $\Delta K_s/K_s$ to the offsets of surface porosity (upper left), subsurface porosity (upper right) in Eq. (3), the H factor (lower left) and subsurface solid component (lower right) in Eq. (13).

(i.e. 6000 samples on the nighttime surface temperature curve). As the discussions above, the estimation error induced by observation number becomes negligible if more than 8 observations are used in the estimation.

As shown in Fig. 10, the uncertainties of surface porosity and subsurface porosity only have very small effects on the estimation error (1.2% and 2.0% respectively). The uncertainty of K_d can result in an estimation error of about 5.0%, which is also acceptable in an inversion problem. So these three parameters can be fixed to their typical values in the estimation. The H factor has a very large perturbation on the estimation accuracy and its influence on the estimation error is more complicated. A 0.04 m increase of H factor results in a relative estimation error of about 25%, whereas a 0.04 m decrease of H factor causes an estimation error as large as 150%!

The estimation errors induced by the uncertainties of surface albedo and emissivity are also quantified in the same manner and shown in Fig. 11. The uncertainties of the parameters in surface albedo model still lack in quantitative constraint. As an alternative choice, we extend the uncertainties of normalized albedo and the coefficients a and b to their individual extreme cases. The typical values of normalized albedo are 0.07 and 0.16 for mare and highland respectively (Vasavada et al., 2012) and we adopt the median value 0.12 as the typical value of normalized surface albedo. In addition, because these two values represent the darkest and the most bright units on the Moon respectively, an uncertainty range ± 0.05 (i.e. half of their difference) should be wide enough. As seen from Fig. 11 (upper left), this uncertainty can induce an estimation error of about 8%, which is basically acceptable in an inversion problem. So this parameter can be fixed to its typical value in the estimation. For the other two empirical coefficients a and b , their uncertainties are assumed as their extreme conditions ± 0.045 and ± 0.14 respectively (i.e. their relative uncertainties are $\pm 100\%$). As the tests shown here, these two parameters can induce a total estimation error of about 17% at lunar equator. Nevertheless, surface albedo is actually a function of solar incident angle and their dependence is controlled by these two coefficients. Thus, their uncertainties will lead to a larger estimation error of about 41% in sum at the latitude 60° .

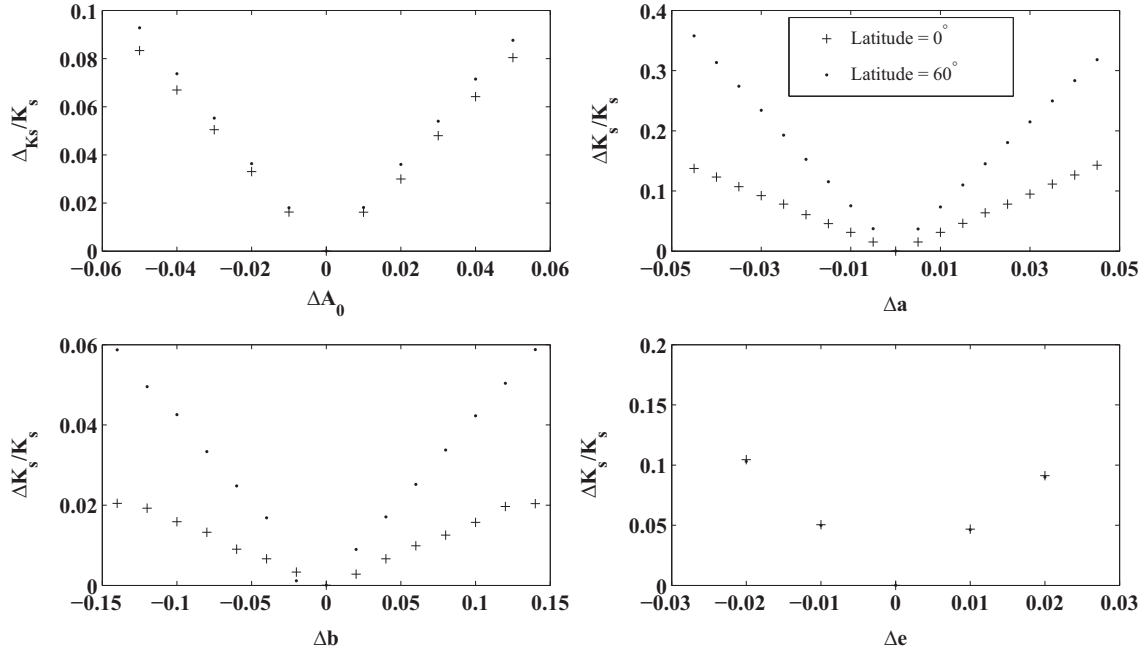


Fig. 11. The sensitivity of estimation error $\Delta K_s/K_s$ to the offsets of normalized surface albedo (upper left), the coefficients a and b (upper right and lower left) in albedo model and surface emissivity (lower right).

The uncertainty of surface emissivity (± 0.01) can only induce an estimation error of about 5%.

3.7. Test on rock abundance

As the increase of rock abundance can substantially elevate the whole level of nighttime surface temperature, this effect will lead to a higher K_s value in the estimation. In order to test the influence of rock debris on the estimation, we will estimate the K_s from the bolometric temperature with the contamination of different amount of rock debris. Here the regolith temperature is simulated by using the typical values shown in Table 1, while the rock temperature is simulated by changing the density and thermal conductivity within skin depth to 3100 kg m^{-3} and $1.5 \text{ W m}^{-1} \text{ K}^{-1}$, respectively. The normalized surface albedo and surface emissivity are fixed as 0.12 and 0.98 respectively. Both slope angle and slope aspect are assumed to be zero.

The test result is shown in Fig. 12. As seen from this figure, the increase of rock abundance is able to elevate the estimated K_s value. Here we truncate the estimated K_s value at $0.0252 \text{ W m}^{-1} \text{ K}^{-1}$ due to the limitations of our temperature model. The numerical solution to heat conductive equation is stable if the time step fulfils von Neumann stability condition (Haberman, 2004)

$$\Delta t \leq \frac{K_{\min} \Delta z^2}{2\rho_{\max} C_{\max}} \quad (30)$$

where K_{\min} is the minimum thermal conductivity, ρ_{\max} is the maximum density, and C_{\max} is the maximum heat capacity. In this test, we set the Δt and Δz to 0.02 lunar hour and 0.01 m respectively, which are adequate for the typical condition of lunar regolith. Nevertheless, because the typical thermal conductivity of rock debris is about 1000 times higher than that of lunar regolith, the simulation of rocky surface temperature requires a much smaller time step. Nevertheless, the decrease of time step will increase the iteration times during a lunation in the individual simulation case. As the temperature simulation will be repeated for hundreds to thousands of times in a least-square fitting, this change will reduce the fitting efficiency substantially. The truncation value actually represents the maximum solid thermal conductivity that can be

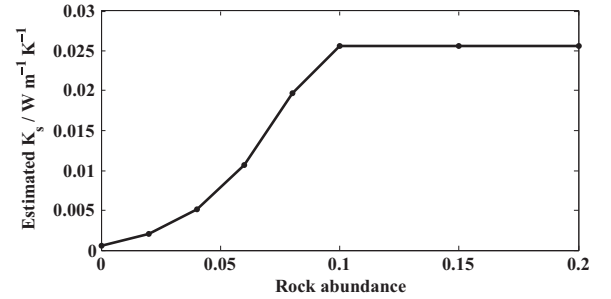


Fig. 12. The influence of rock abundance on the K_s value estimated from bolometric temperature. The rock temperature is simulated by assuming the density and thermal conductivity within skin depth to be 3100 kg m^{-3} and $1.5 \text{ W m}^{-1} \text{ K}^{-1}$ respectively. The estimated K_s is truncated at $0.0252 \text{ W m}^{-1} \text{ K}^{-1}$ because our temperature model cannot be handled with very high rock abundance.

handled at the specified Δt and Δz . In addition, Fig. 12 also indicates that this truncation value corresponds to the rock abundance of about 10%. Therefore, our estimation strategy is not applicable if the rock abundance exceeds about 10%.

4. Result and discussions

4.1. Result and confidence

The estimation result is shown in Fig. 13. The estimated K_s has a wide variation range $0.0001\text{--}0.0300 \text{ W m}^{-1} \text{ K}^{-1}$ between 60°N and 60°S , with an average value of about $0.0007 \text{ W m}^{-1} \text{ K}^{-1}$. The abnormally high K_s values (i.e. far higher than $0.002 \text{ W m}^{-1} \text{ K}^{-1}$) only appear at those young impact craters specified in this figure. Apart from them, the estimated K_s values only vary between 0.0001 and $0.0015 \text{ W m}^{-1} \text{ K}^{-1}$. Specially, the estimated K_s possesses a prominent latitude dependence. In addition, even though there is no prominent mare-highland dichotomy in Fig. 13, the estimated K_s still possesses a variation dominated by the age of surface unit. The estimated K_s in the older regions (e.g. highland and Pre-Nectarian mares) varies between 0.0009 and $0.0012 \text{ W m}^{-1} \text{ K}^{-1}$, whereas the

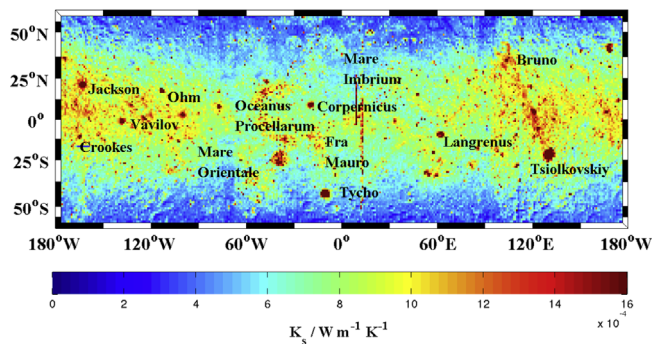


Fig. 13. The distribution of estimated K_s within 60°N and 60°S. The surficial solid thermal conductivity possesses a wide variation range 0.0001–0.0300 $\text{W m}^{-1} \text{K}^{-1}$. The abnormally high solid thermal conductivity (larger than 0.0020 $\text{W m}^{-1} \text{K}^{-1}$) only appears at several young craters specified in the figure.

estimated K_s in those younger surface units (e.g. Mare Imbrium and Mare Orientale) just varies between 0.0005 and 0.0007 $\text{W m}^{-1} \text{K}^{-1}$.

Because the average K_s value is about 0.0007 $\text{W m}^{-1} \text{K}^{-1}$, the parameter tests above are still useful in the evaluation of estimation uncertainty. If the uncertainties of H factor and surface albedo are not considered, the total estimation error induced by other parameters is about 13% in sum. The uncertainty of surface albedo model is not provided in Vasavada et al. (2012) and we do not consider the influence of this parameter here. The uncertainty of H factor has a prominent influence on the estimation accuracy. We have to confess that the estimated K_s values would have coupled the effect of H factor variation. Essentially, the H factor determines the thickness of loosely packed layer beneath the lunar surface. A larger H factor just implies a thicker loosely packed layer in which the heat stored in the subsurface lunar regolith is harder to be transported onto the surface. So the estimated K_s values actually reflect the synthetical heat conduction ability of the near-surface lunar regolith.

In addition, it needs to be clarified that the correlation between thermal conductivity and porosity is not considered in the estimation. The major reason why we do not consider this correlation is that the coefficient f_1 contained in Eq. (12) has too large uncertainty and the correlation between porosity and thermal conductivity cannot be quantified accurately. So the influence of this simplification should also be discussed here. As seen from Fig. 10, the influences of n_s and n_d on the estimated K_s are not so prominent. So the influence of porosity on the solid thermal conductivity does not need to be considered. In addition, the porosity of lunar regolith also affects the radiative part of thermal conductivity. However, given the typical values of nighttime surface temperature (100 K), the variations of n_s and n_d can also perturb radiative part by about $10^{-5} \text{W m}^{-1} \text{K}^{-1}$, which is negligible compared with the range of estimated K_s . So the influence of porosity on the radiative part does not need to be considered neither.

Table 2 shows the comparisons between our estimated K_s values and the previous estimations at several Apollo landing sites. Note that the rock abundances at all these landing sites are far smaller than 1%, so the influence of rock abundance does not need to be considered. Here the previous estimations at those Apollo landing sites are obtained from the laboratory experiments for the regolith samples. As read from this table, the laboratory experiment datum at Apollo 11 landing site is about twice of the estimated K_s in this study. It needs to caution that the laboratory experiment data for this landing site is not sufficiently complete for a critical analysis of the temperature dependence of thermal conductivity (Cremers and Birkebak, 1971). In this case, the separated solid thermal conductivity is not reliable. Apart from the

Table 2

The comparisons between the estimated K_s values and previously measured K_s values at Apollo landing sites.

Site	Location	K_s ($\text{W m}^{-1} \text{K}^{-1}$)	Previously estimated K_s ($\text{W m}^{-1} \text{K}^{-1}$)	Reference
A11	23.6°E, 0.7°N	0.0007	0.0014	Cremers and Birkebak (1971)
A12	23.6°W, 3.0°S	0.0008	0.0009	Cremers and Birkebak (1971)
A15	3.5°E, 26.1°N	0.0007	0.0006	Cremers and Hsia (1974)
A16	15.9°E, 8.9°S	0.0006	0.0005	Cremers and Hsia (1974)

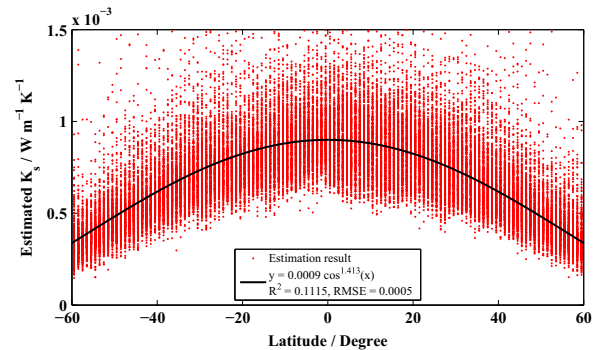


Fig. 14. The estimated K_s values are plotted versus their individual latitudes. It is prominent that the solid thermal conductivity on the lunar surface has strong correlation with latitude.

data at Apollo 11 landing site, our estimated K_s values at Apollo 12, 15 and 16 landing sites are well consistent with the laboratory experiment data in the previous investigations.

Albeit our estimated K_s values are highly consistent with the laboratory experiment data for Apollo returned samples, it needs to caution that those laboratory experiment data cannot represent the realistic conditions on the lunar surface. The experiments in Cremers and Birkebak (1971) and Cremers and Hsia (1974) were carried out by inserting a line heat source into the regolith sample in order to measure the temperature variation over a time period in a certain distance away from the heat source. As a matter of course, the heat source would expand as it heats or bends and perturb the packing style as well as the effective contact area among solid grains. Till now, we have not found any reliable approaches to quantify the error induced by this factor.

4.2. Latitude dependence of K_s

As shown in Fig. 14, the estimated K_s has a prominent latitude dependence. The estimated K_s varies around 0.0009 $\text{W m}^{-1} \text{K}^{-1}$ at lunar equator, while it decreases to about 0.0003 $\text{W m}^{-1} \text{K}^{-1}$ at the latitude 60°. At first, we exclude the possibility that the latitude dependence is caused by the uncertainties of surface albedo and surface emissivity. In our estimation, the surface emissivity and surface albedo are derived from the Diviner observations at lunar equator. If the estimations in the equatorial region were correct and the latitude dependence was caused by the uncertainties of surface albedo and surface emissivity, the K_s at the latitude 60° would have been under-estimated by about 67% on average. As inferred from Fig. 3, the over-estimation of surface emissivity is able to induce the under-estimation of K_s . However, as the emissivity cannot exceed unity, only a 0.02 variation of surface emissivity can only produce an estimation error of about 15%. On the other hand, the over-estimation of surface albedo is

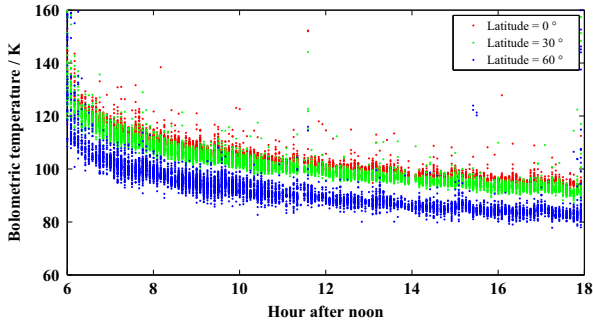


Fig. 15. The bolometric temperature variations in the nighttime at the latitude 0° (red dots), 30° (green dots) and 60° (blue dots) observed by Diviner radiometer. (For interpretation of the references to color in this figure caption, the reader is referred to the web version of this paper.)

able to result in the under-estimation of K_s . The surface albedo is actually a function of solar incident angle whose dependence is controlled by the empirical coefficients a and b therein. Thus, if the K_s was under-estimated in the high latitude region, these two coefficients would have been over-estimated. However, as the tests shown in Fig. 11, the estimation error can only reach as maximum as 41% even though these two coefficients reduce to zero. Therefore, the latitude dependence of K_s should be relative with the intrinsic properties of lunar regolith.

In Eq. (12), we have indicated that solid thermal conductivity also relies on specific surface energy. The specific surface energy should be a function of temperature because the increase of temperature is able to increase the rate of dipoles per molecule (Gundlach and Blum, 2012). So we speculate that the latitude dependence of K_s is a direct consequence of the specific surface energy variation with respect to temperature. In order to verify this speculation, we plot the bolometric temperatures at different latitudes versus local time in Fig. 15. As seen from here, the whole temperature level at the latitude 30° is about 5 K lower than the lunar equator, while the whole temperature level at the latitude 60° is about 20 K lower than the lunar equator. Therefore, the variation of whole temperature level with respect to latitude is able to perturb specific surface energy, which produces the variation of K_s with respect to latitude. Nevertheless, because there is still no certain theory to constrain the relation between specific surface energy and temperature, the quantitative verification on this speculation still requires the supports from future experiments.

4.3. Dichotomy of K_s distribution

In order to enhance the dichotomy of K_s distribution, the estimated K_s values are normalized for latitude following the fitted relation in Fig. 14. The distribution of normalized K_s is shown in Fig. 16. As seen from this figure, the normalized K_s in some older regions (e.g. highland, South-Pole Aitken, Nectaris) varies around $0.0010 \text{ W m}^{-1} \text{ K}^{-1}$, whereas the normalized K_s in those younger regions (e.g. Imbrium and Orientale) only varies around $0.0005 \text{ W m}^{-1} \text{ K}^{-1}$. Except Oceanus Procellarum, the rock abundance in these regions is far smaller than 1%, so rock abundance is not the predominant factor to induce the variation of K_s . The higher K_s value in Oceans Procellarum would correlate with the higher rock abundance (about 1%). In this analysis, we do not take this region into consideration.

One possibility is that the variation of normalized K_s is caused by the grain radius variation across the entire lunar surface. Eq. (14) has implied that solid thermal conductivity is inversely proportional to $r^{1/3}$. Therefore, those regions with smaller grain radius should have higher solid thermal conductivity. Because the older

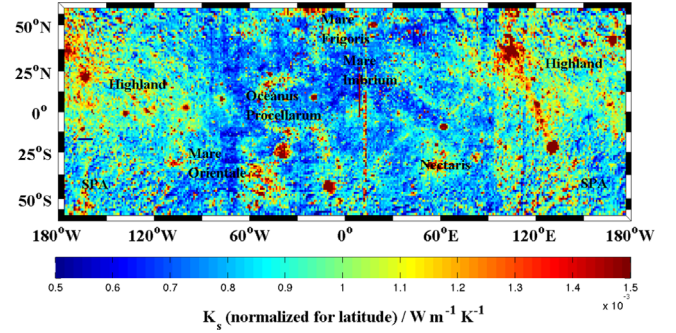


Fig. 16. The estimated K_s values within 60°N and 60°S are normalized for latitude in order to enhance the variation of K_s in the longitude direction.

regions have experienced longer gardening and space weathering history, the lunar regolith there should be crushed more severely. As the consequence, the older regions should have higher normalized K_s .

It also needs to note that the estimated K_s also couples the effect of H factor variation, but this factor cannot hinder us to obtain the conclusion above. Because H factor is inversely proportional to $r^{3/4}$, the smaller grain radius in the older regions is able to result in larger H factor. In fact, the increase of H factor can reduce the whole level of nighttime surface temperature, which leads to a smaller K_s in the estimation. Therefore, the normalized K_s values in the older regions have been under-estimated. Similarly, the younger regions should have larger grain radius and smaller H factor. In this case, the normalized K_s have been over-estimated. Therefore, the realistic K_s variation across the younger and older regions would be more drastic than that shown in Fig. 16.

4.4. Abnormally high K_s at young craters

The estimated K_s values at several young craters are abnormally higher than other regions. We list these craters as well as their estimated K_s , rock abundances and absolute ages in Table 3. Here the K_s values are sampled at the center of these craters where the estimated K_s is highest. The rock abundances and absolute ages of these craters are calculated from the anisothermality across the wavelength (Bandfield et al., 2011) and crater counting technique respectively. As seen from this table, all these craters have very high rock abundances. Therefore, the abnormally high K_s values at these craters are possibly relative with the enrichment of rock debris on the surface.

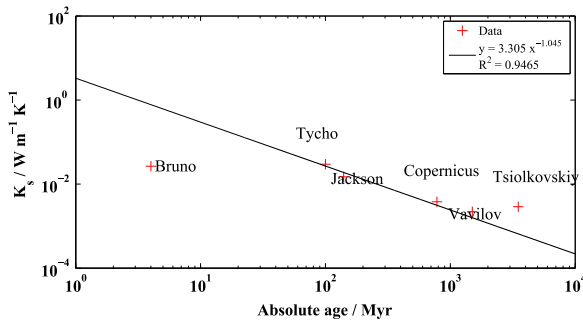
To verify this speculation, the correlation between the estimated K_s and the absolute ages of these craters should be checked. The gardening and space weathering can reduce the amount of rock debris on the lunar surface (Hörz et al., 1975). In addition, Ghent et al. (2014) and Ghent et al. (2016) also yield a similar conclusion in which the rock abundance estimated from Diviner data at young craters correlate with their absolute ages negatively. Based upon them, if the abnormally high K_s values at these craters were caused by the enrichment of rock debris, their estimated K_s values should also have a negative correlation with their absolute ages.

As shown in Fig. 17, the estimated K_s values at these craters are plotted versus their absolute ages. In order to check the correlation between these two quantities, the ill-posed data points should be excluded at first. According to the tests above, the estimated K_s becomes saturated when rock abundance exceeds 10%. This phenomenon also occurs in the estimation result. For example, although the rock abundance at Bruno (14.5%) is far larger than Tycho (4.1%), the estimated K_s values at these two craters are still similar. So the estimated K_s value at Bruno should have saturated.

Table 3

The rock abundance, surficial solid component and absolute age of the craters with abnormally high surficial solid component.

Crater	Location	K_s ($\text{W m}^{-1} \text{K}^{-1}$)	Rock abundance (%)	Age	Reference
Jackson	163.5°W, 22.5°N	0.0149	2.9	140 Ma	Bogert et al. (2010)
Crookes	164.5°W, 10.5°S	0.0096	2.3	–	–
Vavilov	138.5°W, 0.5°N	0.0022	1.7	1.5 Ga	Kirchoff et al. (2013)
Ohm	113.5°W, 18.5°N	0.0102	2.7	–	–
Copernicus	113.5°W, 10.5°N	0.0038	3.1	782 Ma	Hiesinger et al. (2012)
Tycho	10.5°W, 43.5°S	0.0250	4.1	100 Ma	Hiesinger et al. (2012)
Langrenus	62.5°E, 8.5°S	0.0020	1.0	–	–
Bruno	103.5°E, 35.5°N	0.0252	14.5	4 Ma	Morota et al. (2009)
Tsiolkovskiy	129.5°E, 20.5°S	0.0029	3.2	3.5 Ga	Tyrie (1988)

**Fig. 17.** The estimated K_s values at young craters are plotted versus their absolute ages. There is a prominent negative correlation between the estimated K_s value and absolute age.

To avoid this problem, we give the best fitted relation between these two quantities by excluding the data point of Bruno. As seen from this figure, the estimated K_s values at these young craters do have strong negative correlation with their absolute ages. Consequently, the abnormally high K_s values at these craters should be dominated by the enrichment of rock debris.

Because the estimated K_s values at young craters contain chronological information, the absolute ages of young craters can be determined from the fitted relation in Fig. 17. For example, the K_s values at Crookes and Ohm are determined as 0.0096 and 0.0102 $\text{W m}^{-1} \text{K}^{-1}$ respectively. Based upon the fitted relation shown in Fig. 17, the absolute ages of Crookes and Ohm can be predicted as 268 and 252 Myr respectively. These two ages still require the future verifications from crater counting.

The K_s reduction versus absolute age tends to be not prominent after 1.0 Gyr. Due to this reason, the absolute ages of these craters cannot be accurately resolved from the K_s versus absolute age plot. For example, although crater counting shows that Tsiolkovskiy is much older than Vavilov, the estimated K_s value at Vavilov (0.0022 $\text{W m}^{-1} \text{K}^{-1}$) is still similar to Tsiolkovskiy (0.0029 $\text{W m}^{-1} \text{K}^{-1}$). In addition, the absolute age of Tsiolkovskiy obtained by crater counting would have been over-estimated due to the discovery of impact melt sheet around this crater (Neish et al., 2013). So the absolute age of Tsiolkovskiy is still uncertain. As there are only two data points after 1.0 Gyr, we cannot ensure the accuracy of our fitted relation in this regime. Therefore, the absolute ages of those craters with the estimated K_s value around 0.002 $\text{W m}^{-1} \text{K}^{-1}$ (e.g. Langrenus) cannot be determined accurately.

5. Conclusions

The thermal conductivity of lunar regolith is a critical parameter in the global heat flow estimation and understanding the nature of surface materials. In this study, the solid thermal conductivity on the surface (K_s) is estimated from the bolometric temperature dataset generated from Diviner observations. Our estimation shows that K_s has a wide variation range 0.0001–

0.0300 $\text{W m}^{-1} \text{K}^{-1}$ between 60°N and 60°S. The estimated K_s possesses a prominent latitude dependence, which is suggested to be the consequence of the specific surface energy variation with respect to temperature. However, because there is still no certain theory to quantify the relation between specific surface energy and temperature, this speculation still requires the supports from future experiments.

In addition, even though the distribution of K_s does not have prominent mare-highland dichotomy, we still find that the distribution of K_s is dominated by the absolute ages of surface units. The estimated K_s values in the older regions are ubiquitously higher than those in the younger regions. This phenomenon would be relative with the variation of grain radius across the entire lunar surface. The older regions have experienced longer gardening and space weathering history, which will lead to smaller grain radius and higher solid thermal conductivity in turn.

The surficial solid thermal conductivity values at young impact craters are abnormally higher than other regions. This phenomenon would be relative with the enrichment of rock debris on the lunar surface. The estimated K_s at these young craters also show a strong negative correlation with their absolute ages, which would be relative with the effects of gardening and space weathering on the surface. Thus, the estimated surficial solid thermal conductivity also contains the chronological information. Based upon the fitted relation between surficial solid component and absolute age, the absolute ages of Crookes and Ohm are estimated as 268 and 252 Myr respectively. The reduction of K_s tends to be not prominent after 1.0 Gyr. In this case, the absolute age of crater cannot be accurately resolved from the fitted relation between estimated K_s and absolute age.

We also propose two important issues in our future investigations in order to improve our estimation result, including (1) more knowledge about the intrinsic properties of lunar regolith should be known. In order to decouple the effects of K_s and H factor from Diviner observations, the estimation of grain radius should be a better option. However, because K_s also relies on specific surface energy, the relation between specific surface energy and temperature also requires to be realized in advance. Till now, there is no certain theory to constrain this relation; (2) the convergence theory of Nelder–Mead algorithm. Because lunar surface temperature is calculated numerically, the least-square fitting between simulated surface temperature and Diviner data has to be performed by this simplex search algorithm. In fact, the convergence of the simplex search with multiple free parameters is still poorly understood. This problem should also be handled in the future.

Acknowledgments

The authors are very thankful to M.A. Siegler and Paul O. Hayne (Jet Propulsion Laboratory) for the suggestions on the temperature

model and the usage of Diviner data. This research is jointly sponsored by the Science and Technology Development Fund of Macau SAR (080/2012/A3), National Natural Science Foundation of China (No. 11203002), Open Fund of the Key Planetary Sciences (No. PSL1403) and PKU PRSL contribution 8.

References

- Bandfield, J.L., Ghent, R.R., Vasavada, A.R., Paige, D.A., Lawrence, S.J., Robinson, M.S., 2011. Lunar surface rock abundance and regolith fines temperatures derived from Iro diviner radiometer data. *J. Geophys. Res.*, 116.
- Bandfield, J.L., Hayne, P.O., Williams, J.P., Greenhagen, B.T., Paige, D.A., 2015. Lunar surface roughness derived from Iro diviner radiometer observations. *Icarus* 248, 357–372.
- Bogert, C.H.V.D., Hiesinger, H., McEwen, A.S., Dundas, C., Bray, V., Robinson, M.S., Plescia, J.B., Reiss, D., Klemm, K., Bogert, C.H.V.D., 2010. Discrepancies between crater size-frequency distributions on ejecta and impact melt pools at lunar craters: an effect of differing target properties? In: Lunar and Planetary Science Conference, p. 2165.
- Cao, W., Cai, Z., Tang, Z., 2015. Fractal structure of lunar topography: an interpretation of topographic characteristics. *Geomorphology* 238, 112–118.
- Carrier, W.D., Olhoeft, G.R., Mendell, W., 1991. Physical properties of the lunar surface. In: Lunar Sourcebook, pp. 475–594.
- Cremers, C., Hsia, H., 1974. Thermal conductivity of Apollo 16 lunar fines. In: Lunar and Planetary Science Conference Proceedings, pp. 2703–2708.
- Cremers, C.J., Birkebæk, R.C., 1971. Thermal conductivity of fines from Apollo 12. In: Lunar and Planetary Science Conference Proceedings, p. 2311.
- Ghent, R.R., Carter, L.M., Bandfield, J.L., 2016. Lunar crater ejecta: physical properties revealed by radar and thermal infrared observations. *Icarus* . <http://dx.doi.org/10.1016/j.icarus.2015.12.014>.
- Ghent, R.R., Hayne, P.O., Bandfield, J.L., Campbell, B.A., Allen, C.C., Carter, L.M., Paige, D.A., 2014. Constraints on the recent rate of lunar ejecta breakdown and implications for crater ages. *Geology* 42, 1059–1062.
- Grott, M., Knollenberg, J., Krause, C., 2010. Apollo lunar heat flow experiment revisited: a critical reassessment of the in situ thermal conductivity determination. *J. Geophys. Res.: Planets*, 115.
- Gundlach, B., Blum, J., 2012. Outgassing of icy bodies in the solar system-II: heat transport in dry, porous surface dust layers. *Icarus* 219, 618–629.
- Gundlach, B., Blum, J., 2013. A new method to determine the grain size of planetary regolith. *Icarus* 223, 479–492.
- Güttler, C., Krause, M., Geretshauser, R.J., Speith, R., Blum, J., 2009. The physics of protoplanetary dust agglomerates. iv. toward a dynamical collision model. *Astrophys. J.* 701, 130.
- Haberman, R., 2004. Applied partial differential equations with fourier series and boundary value problems. *AMC* 10, 12.
- Hayne, P.O., Ghent, R., Bandfield, J.L., Vasavada, A.R., Siegler, M.A., Greenhagen, B.T., Williams, J.P., Paige, D.A., 2013. Formation and evolution of the moon's upper regolith: constraints from diviner thermal measurements. In: Lunar and Planetary Science Conference Abstracts, p. 3003.
- Hemingway, B.S., Robie, R., Wilson, W., 1973. Specific heats of lunar soils, basalt, and breccias from the Apollo 14, 15 and 16 landing sites, between 90 and 350 K. In: Lunar and Planetary Science Conference Proceedings, p. 2481.
- Hiesinger, H., Bogert, C., Pasckert, J., Funcke, L., Giacomini, L., Ostrach, L., Robinson, M., 2012. How old are young lunar craters? *J. Geophys. Res.*, 117.
- Hörz, F., Schneider, E., Gault, D.E., Hartung, J.B., Brownlee, D.E., 1975. Catastrophic rupture of lunar rocks: a Monte Carlo simulation. *Moon* 13, 235–258. <http://dx.doi.org/10.1007/BF00567517>.
- Huang, Q., Wieczorek, M.A., 2012. Density and porosity of the lunar crust from gravity and topography. *J. Geophys. Res.*, 117.
- Jaeger, J.C., 1953. The surface temperature of the moon. *Aust. J. Phys.* 6, 10–21.
- Keihm, S.J., 1984. Interpretation of the lunar microwave brightness temperature spectrum: feasibility of orbital heat flow mapping. *Icarus* 60, 568–589.
- Kirchoff, M.R., Chapman, C.R., Marchi, S., Curtis, K.M., Enke, B., Bottke, W.F., 2013. Ages of large lunar impact craters and implications for bombardment during the moon's middle age. *Icarus* 225, 325–341.
- Lagarias, J.C., Reeds, J.A., Wright, M.H., Wright, P.E., 1998. Convergence properties of the nelder-mead simplex method in low dimensions. In: *SIAM J. Optim.* 112–147.
- Langseth, M.G., Keihm, S.J., Peters, K., 1976. Revised lunar heat-flow values. In: Lunar and Planetary Science Conference Proceedings, pp. 3143–3171.
- Lucey, P.G., Taylor, G.J., Malaret, E., 1995. Abundance and distribution of iron on the moon. *Science* 268, 1150–1153.
- Miyahara, H., Wen, G., Cahalan, R.F., Ohmura, A., 2008. Deriving historical total solar irradiance from lunar borehole temperatures. *Geophys. Res. Lett.*, 35.
- Morota, T., Haruyama, J., Miyamoto, H., Honda, C., Ohtake, M., Yokota, Y., Matsunaga, T., Hirata, N., Demura, H., Takeda, H., 2009. Formation age of the lunar crater Giordano Bruno. *Meteorit. Planet. Sci.* 44, 1115–1120.
- Neish, B., Patterson, G., Cahill, J., Bandfield, J., Petro, N., Hawke, B., 2013. Impact melt deposits at Tsiolkovskiy crater: constraints on crater age. cd. In: Lunar and Planetary Science Conference Abstracts, p. 1585.
- Nelder, J.A., Mead, R., 1965. A simplex method for function minimization. *Comput. J.* 7 (7), 308–313.
- Paige, D., Foote, M., Greenhagen, B., Schofield, J., Calcutt, S., Vasavada, A., Preston, D., Taylor, F., Allen, C., Snook, K., et al., 2010. The lunar reconnaissance orbiter diviner lunar radiometer experiment. *Space Sci. Rev.* 150, 125–160.
- Presley, M.A., Christensen, P.R., 1997. Thermal conductivity measurements of particulate materials 1. a review. *J. Geophys. Res.* 102, 6535–6549.
- Prettyman, T., Hagerty, J., Elphic, R., Feldman, W., Lawrence, D., McKinney, G., Vaniman, D., 2006. Elemental composition of the lunar surface: analysis of gamma ray spectroscopy data from lunar prospector. *J. Geophys. Res.*, 111.
- Robie, R.A., Hemingway, B.S., Wilson, W.H., 1970. Specific heats of lunar surface materials from 90 to 350 degrees kelvin. *Science* 167, 749–750.
- Rosenburg, M., Aharonson, O., Head, J., Kreslavsky, M., Mazarico, E., Neumann, G.A., Smith, D.E., Torrence, M.H., Zuber, M.T., 2011. Global surface slopes and roughness of the moon from the lunar orbiter laser altimeter. *J. Geophys. Res.*, 116.
- Schräpler, R., Blum, J., von Borstel, L., Güttler, C., 2015. The stratification of regolith on celestial objects. *Icarus* 257, 33–46.
- Tyrie, A., 1988. Age dating of mare in the lunar crater Tsiolkovskiy by crater-counting method. *Earth Moon Planets* 42, 245–264.
- Vasavada, A.R., Bandfield, J.L., Greenhagen, B.T., Hayne, P.O., Siegler, M.A., Williams, J.P., Paige, D.A., 2012. Lunar equatorial surface temperatures and regolith properties from the diviner lunar radiometer experiment lunar equatorial surface temperatures and regolith properties from the diviner lunar radiometer experiment. *J. Geophys. Res.: Planets*, 117. <http://dx.doi.org/10.1029/2011JE003987>.
- Williams, J.P., Sefton-Nash, E., Paige, D.A., 2015. The temperatures of Giordano Bruno crater observed by the diviner lunar radiometer experiment: application of an effective field of view model for a point-based data set. *Icarus*, in press.